High-temperature superconductivity in SrB_3C_3 and BaB_3C_3 predicted from first-principles anisotropic Migdal-Eliashberg theory

Jin-Ning Wang,[1] Xun-Wang Yan,[2] and Miao Gao[1,*]

[1]*Department of Physics, School of Physical Science and Technology, Ningbo University, Zhejiang 315211, China*

[2]*College of Physics and Engineering, Qufu Normal University, Shandong 273165, China*

(Received 27 January 2021; accepted 9 April 2021; published 19 April 2021)

Very recently, carbon-boron clathrate SrB_3C_3 has been successfully synthesized, in which carbon and boron atoms form sp^3-bonded truncated octahedral cages. Interestingly, the sp^3-hybridized σ-bonding bands are partially occupied. This may drive SrB_3C_3 into a superconducting state, like boron-doped diamond. By means of density functional first-principles calculations and Wannier interpolation technique, we have investigated the electron-phonon coupling and phonon-mediated superconductivity in SrB_3C_3. Our calculations reveal that there exists strong coupling between sp^3-hybridized σ-bonding bands and boron-associated E_g phonon modes. Based on the Migdal-Eliashberg theory, we self-consistently solve the anisotropic Eliashberg equations. It is found that SrB_3C_3 is a single-gap superconductor, with superconducting transition temperature being 40 K. The anisotropic ratio of superconducting energy gap is computed to be 32.8%. Further replacing Sr with Ba, the transition temperature can be boosted to 43 K in BaB_3C_3 due to phonon softening. These findings suggest that SrB_3C_3 and BaB_3C_3 are phonon-mediated high-temperature anisotropic *s*-wave superconductors.

DOI: 10.1103/PhysRevB.103.144515

I. INTRODUCTION

Diamond is an indirect-gap insulator with the gap value being 5.5 eV [1]. In 2004, it was first reported that boron-doped diamond synthesized at high pressure (8–9 GPa) and high temperature (2500–2800 K) is a superconductor, with transition temperature (T_c) close to 4 K [2]. The boron content that incorporated into diamond is about 2.8% [2]. On the origin of metallicity of boron-doped diamond, angle-resolved photoemission spectroscopy (ARPES) measurements confirmed that the charge carriers were introduced into the sp^3-hybridized σ-bonding bands of diamond [3]. Based on virtual-crystal approximation (VCA), it was shown by density-functional theory (DFT) studies that the coupling between σ-bonding valence band and optical bond-stretching zone-center phonons is quite strong, and the deformation potential caused by zone-center bond-stretching phonon modes is at least 60% larger than in MgB_2 [4,5]. This suggested that heavily boron-doped diamond is a three-dimensional MgB_2-type superconductor. Beyond VCA, the local vibration of boron atom plays an essential role in electron-phonon coupling (EPC) as revealed by supercell computations [6,7]. In particular, the EPC constant λ and T_c were determined to be 0.39 and 4.4 K, respectively, in excellent agreement with experiment [7]. Compared with MgB_2, the reason for weaker EPC and lower T_c in boron-doped diamond was attributed to the smaller density of states (DOS) at the Fermi level [5–7].

Therefore, increasing the boron concentration is a straightforward way to boost the T_c [8]. Indeed, boron concentration can be promoted to 5% in diamond films via microwave plasma-assisted chemical vapor deposition method, yielding a T_c of 11.4 K [9]. As we know, boron cannot sustain the diamond structure [10]. This indicates that heavier boron doping may trigger structural phase transition, owing to strong EPC. Although several diamondlike compounds with large boron content have been synthesized, exemplified by BC_5 [11] and BC_3 [12], the evidence for superconductivity in these materials is still unavailable. To date, even higher boron concentration in diamond, such as B:C equal to 1:1, has never been achieved.

For carbon, diamond is the unique sp^3-bonded structure at ambient pressure. As the nearest neighbor of carbon in group-IV elements, silicon takes diamond structure as its ground state. However, aside from the diamond structure, all silicon atoms in cagelike silicon clathrate are also covalently bonded within a four-neighbor sp^3 environment [13]. Particularly, it was found that $(Na,Ba)_xSi_{46}$ and Ba_8Si_{46}, which consist of Si_{20} and Si_{24} cages, can become phonon-mediated superconductors at 4 K and 8 K, respectively [14–16]. Motivated by the superconductivity in silicon clathrate, EPC in carbon clathrates under either *n*-type or *p*-type doping was theoretically investigated [17,18]. Similar to boron-doped diamond, *p*-type doping was expected to drive carbon clathrate into a high-T_c state [18]. Nevertheless, carbon clathrate has never been produced in experiment. Very recently, with the guiding from particle-swarm structure prediction method [19], Zhu *et al.* successfully synthesized a thermodynamically stable carbon-boron sp^3-bonded clathrate, namely SrB_3C_3 [20]. SrB_3C_3 is composed of a cagelike carbon-boron truncated octahedron with alternating C and B atoms at the vertices of the cage and an intercalated Sr atom at the cage center (Fig. 1). As shown by DFT calculations, the sp^3-hybiridized σ-bonding bands are partially filled, due to one-electron short

*gaomiao@nbu.edu.cn

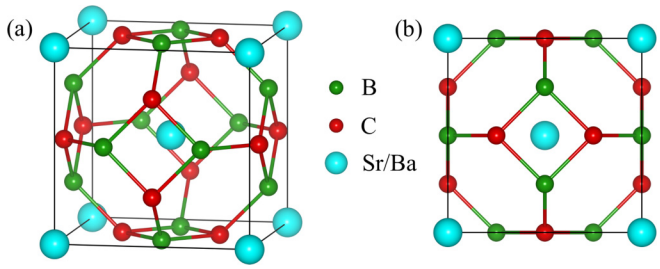

FIG. 1. Crystal structures for SrB_3C_3 and BaB_3C_3. (a) Three-dimensional view. (b) View along the [100] direction. The cyan, green, and red balls represent strontium/barium, boron, and carbon atoms, respectively. The solid black line denotes the unit cell.

in the intercalant [20]. Based on these observations, SrB_3C_3 clathrate is an analog of heavily boron-doped diamond with B:C ratio being 1:1. So, it is quite interesting to know whether SrB_3C_3 clathrate is a high-T_c superconductor.

It is known that MgB_2 is a two-band high-T_c superconductor, associated with the partially occupied metallic σ and π bands [21–23]. According to previous calculations, SrB_3C_3 has three incompletely filled bands [20]. Although, the T_c of SrB_3C_3 has been evaluated via the McMillian-Allen-Dynes formula [24], it is critical to investigate the influence of multiband effect on EPC and phonon-mediated superconductivity of SrB_3C_3 by self-consistently solving the anisotropic Eliashberg equations. In this work, based on first-principles calculations in combination with Wannier interpolation, we have investigated the electronic structure, lattice dynamics, and EPC in SrB_3C_3 and isostructural BaB_3C_3. Our calculations reveal that the EPC mainly comes from the coupling between C-2p orbitals and boron E_g phonon modes. The strengths of EPC are computed to be 0.92 and 0.96 for SrB_3C_3 and BaB_3C_3, respectively. The enhanced EPC in BaB_3C_3 is resulted from softened phonons. By solving the anisotropic Eliashberg equations, the strong EPC can pair electrons into high-T_c states, with transition temperatures being 40 K and

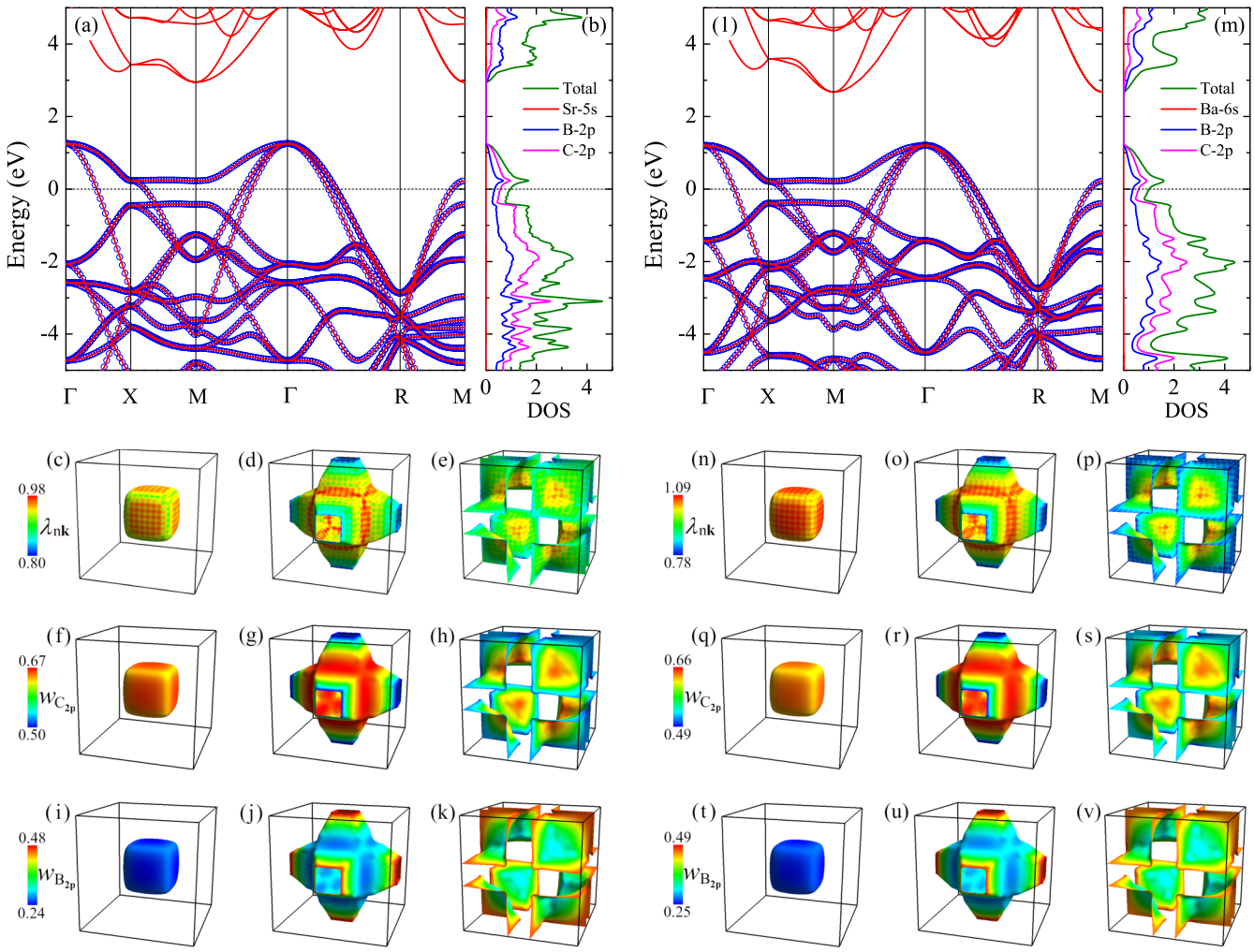

FIG. 2. (a)–(k) Electronic structure for SrB_3C_3. (a) Band structure. The red lines and blue circles denote the bands obtained by first-principles calculation and interpolating the real-space Hamiltonian, respectively. The Fermi level is set to zero. (b) Total and orbital-resolved DOS. The unit for DOS is states/spin/eV/cell. (c)–(e) Fermi surfaces, whereas the colors stand for the strength of EPC $\lambda_{\mathbf{k}n}$. (f)–(h) The weights of C-2p orbitals on the Fermi surfaces. (i)–(k) The weights of B-2p orbitals on the Fermi surfaces. (l)–(v) Electronic structure for BaB_3C_3.

43 K for SrB_3C_3 and BaB_3C_3. At 5 K, the average superconducting gap and anisotropic ratio are computed as 6.31 meV and 32.8% in SrB_3C_3. In particular, these two quantities further increase to 7.09 meV and 34.7% in BaB_3C_3. Our solid calculations suggest that sp^3-hybridized boron-carbon compound, with B:C ratio being 1:1, can achieve a high-T_c state above 40 K.

II. RESULTS AND DISCUSSIONS

Figure 1 shows the crystal structure for SrB_3C_3. Sr atoms occupy the center of cage-like carbon-boron truncated octahedron. The lattice constant for SrB_3C_3 is optimized to 4.8776 Å, in excellent agreement with the experiment [20]. The calculated band structure, partial DOS, and Fermi surfaces of SrB_3C_3 are presented in Fig. 2. As confirmed by our calculation, SrB_3C_3 is inherently metallic, with three bands crossing the Fermi level [Fig. 2(a)]. There is an indirect gap of 1.70 eV. The first-principles band structure is well reproduced by interpolating the real-space Hamiltonian generated by MLWFs. This pledges the validity of subsequent MLWFs-based interpolation and unambiguously proves that the partially filled bands are sp^3-hybridized bonding bands. The C-2p orbitals have larger contribution to the DOS around the Fermi level [Fig. 2(b)], owing to stronger electronegativity of carbon with respect to boron. On the contrary, the DOS of empty bands, i.e., the antibonding bands, is dominated by B-2p orbitals. Interestingly, the dispersion for partially occupied bands along the high-symmetry X-M direction is quite small, giving rise to a Van Hove singularity in the DOS. There are three holelike Fermi surfaces, including a cubic pocket [Fig. 2(c)], a multiterminal tube [Fig. 2(d)], and eight Fermi sheets around the Brillouin zone corner [Fig. 2(e)]. After mapping the momentum **k**- and band index n-resolved EPC constant $\lambda_{\mathbf{k}n}$ on the Fermi surfaces, we find that the distribution of $\lambda_{\mathbf{k}n}$ is of certain anisotropy. It is noteworthy that the weight of C-2p orbitals on Fermi-surface states behaves similarly to $\lambda_{\mathbf{k}n}$ [Figs. 2(f)–2(k)]. This suggests that electronic states associated with C-2p orbitals have strong coupling with phonons.

The lattice constant of BaB_3C_3 is 5.0138 Å, which expands 2.79% compared with SrB_3C_3. Consequently, the hopping integrals are reduced, leading to the decrease of band widths and increase of DOS at the Fermi level [Fig. 2(l)]. Specifically, $N(0)$, DOS at the Fermi level, is equal to 1.04 states/spin/eV/cell in BaB_3C_3 and 0.97 states/spin/eV/cell in SrB_3C_3. Because the contribution of alkaline earth metals to $N(0)$ is negligible in SrB_3C_3, BaB_3C_3, and MgB_2, we can quantificationally compare the $N(0)$ in these systems, as well as in boron-doped diamond. In particular, we utilize the modified $N(0)$, namely $N_2(0)$, whose unit is states/spin/eV/"two atoms cell" [6]. Here, only boron and carbon atoms are taken into consideration when countering the number of atoms. For SrB_3C_3, BaB_3C_3, and MgB_2, $N_2(0)$ equals to 0.16, 0.17, and 0.36 [25,26] states/spin/eV/"two atoms cell," respectively. As a comparison, $N_2(0)$ lies in 0.06–0.07 states/spin/eV/"two atoms cell" for 2.5–3.0% boron-doped diamond [4,5,7]. Although, $N_2(0)$ of SrB_3C_3 is just about half that of MgB_2, it is already more than twice that of boron-doped diamond. The Fermi surfaces of BaB_3C_3 are almost the same as that of

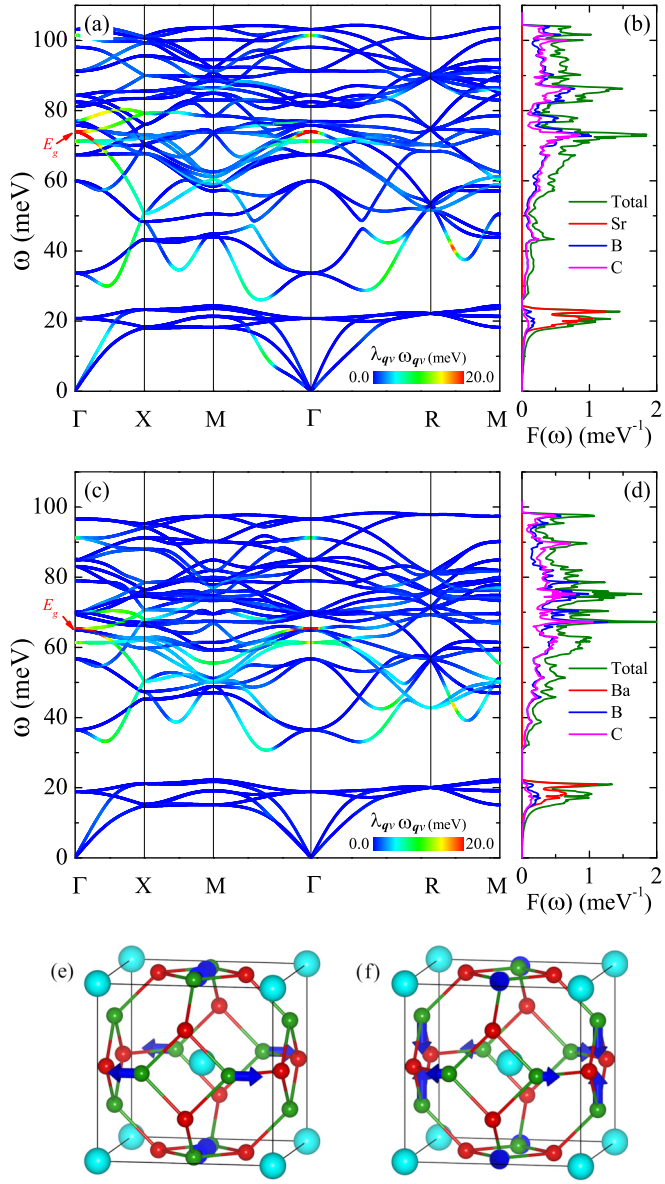

FIG. 3. Lattice dynamics of SrB_3C_3 and BaB_3C_3. Phonon spectrum with a color representation of $\lambda_{\mathbf{q}v}\omega_{\mathbf{q}v}$ for (a) SrB_3C_3 and (c) BaB_3C_3. E_g are the strongly coupled phonon modes. Projected phonon DOS generated by quasiharmonic approximation for (b) SrB_3C_3 and (d) BaB_3C_3. (e)–(f) Phonon displacements for double degenerate E_g modes at the Γ point. The displacements are denoted by blue arrows.

SrB_3C_3. But, the rise of EPC strength can be clearly observed according to Figs. 2(n)–2(p). The weights of C-2p and B-2p orbitals on the Fermi surface remain unchanged [Figs. 2(q)–2(v)], with respect to SrB_3C_3.

Figure 3 shows the lattice dynamics of SrB_3C_3 and BaB_3C_3, whose stabilities are ascertained by the nonimaginary phonon spectra [Figs. 3(a) and 3(c)]. The occupation of σ-bonding bands is critical to the stability of the compound. For example, the σ-bonding bands of graphene lie about 3 eV below the Fermi level [27]. In contrast, free-standing honeycomb borophene does not exist because of the limited occupation of σ bands [28]. Although honeycomb borophene

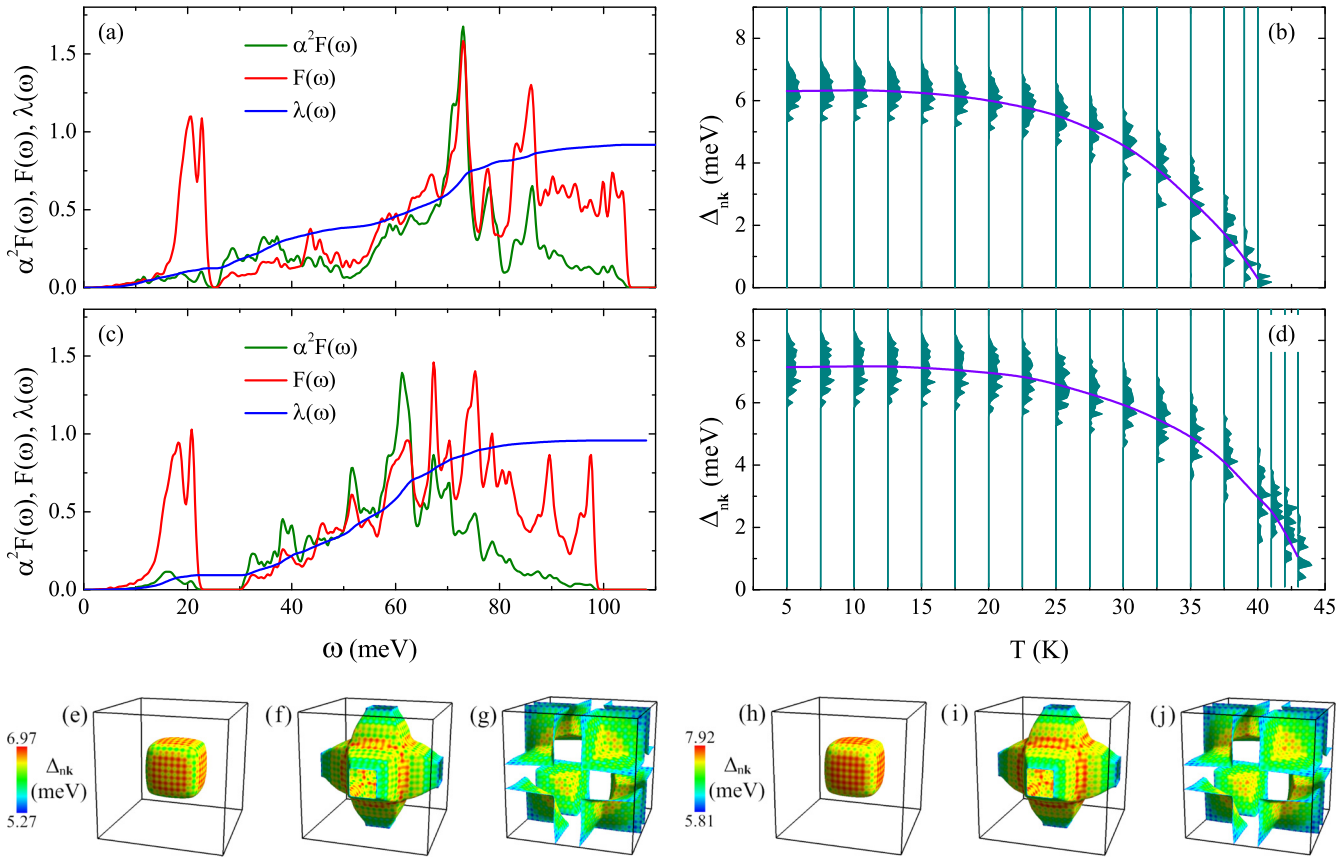

FIG. 4. (a) Phonon DOS $F(\omega)$, Eliashberg spectral function $\alpha^2F(\omega)$, and accumulated $\lambda(\omega)$ for SrB_3C_3. (b) Normalized superconducting gap distributions of SrB_3C_3 at different temperatures. (c) $F(\omega)$, $\alpha^2F(\omega)$, and $\lambda(\omega)$ for BaB_3C_3. (d) Normalized superconducting gap distributions of BaB_3C_3. $\lambda(\omega)$ is computed using the formula $2\int_0^{\omega}\frac{1}{\omega'}\alpha^2F(\omega')d\omega'$. The graduation of $F(\omega)$ is omitted for clarity. The violet lines in (c) and (d) represent the average $\Delta_{\mathbf{k}n}$ for each temperature. (e)–(g) Distributions of superconducting gap $\Delta_{\mathbf{k}n}$ on Fermi surfaces for SrB_3C_3 at 5 K. (h)–(j) Distributions of superconducting gap $\Delta_{\mathbf{k}n}$ on Fermi surfaces for BaB_3C_3 at 5 K. The screened Coulomb potential μ^* is set to 0.1.

has been grown on the Al(111) surface [29], it was found that the charge transfer from Al substrate is of extreme importance to stabilize the honeycomb structure [29,30]. Similarly, it was reported that the Sr atom transfers 1.32 electrons to the boron-carbon clathrate [24]. This plays a vital role in holding the structure of SrB_3C_3. As evidence, we calculate the lattice vibration of RbB_3C_3, which is one electron short compared with SrB_3C_3. This means the occupation of σ bands will be further reduced. We find that the phonon spectrum of RbB_3C_3 has substantial imaginary frequencies, with the maximal one being -25.20 meV. For SrB_3C_3, there is a small frequency gap around 25 meV, with the gap value being 2.42 meV [Fig. 3(a)]. A DOS peak can be clearly seen just below the gap, due to nearly dispersionless phonon modes. These phonon modes are attributed to the vibrations of Sr atoms, as indicated by the projected phonon DOS obtained through quasiharmonic approximation [Fig. 3(b)]. Double degenerate phonon modes E_g at the Γ point possess strong coupling with electrons. Besides E_g modes, the acoustic modes between M and Γ points also have sizable coupling strength. To identify which element can have dominant contribution to the EPC in the frequency interval 0–25 meV, we calculate the phonon displacement for $\mathbf{q}$ being (M-Γ)/2. We find that all the atoms participate in the acoustic B_1 phonon mode, but the amplitudes of boron and carbon atoms are significantly larger than that of Sr atoms. Thus, boron and carbon atoms possess dominant contribution to EPC even in 0–25 meV. After the substitution of Ba for Sr, the frequency gap expands to 8.99 meV [Fig. 3(c)]. Basically, the vast majority of phonon modes show slight softening, for example, the frequency of E_g modes decrease from 73.97 meV to 65.33 meV. However, phonon modes around 40 meV are abnormally hardened. The frequencies of modes below the gap are almost unaffected. The strongly coupled acoustic modes disappear in BaB_3C_3. Although boron and carbon atoms have almost equal contribution to the phonon DOS [Figs. 3(b) and 3(d)], the E_g modes mainly involve the movements of boron atoms within the boundary faces of the cubic cell [Figs. 3(e) and 3(f)]. Hence, the EPC of SrB_3C_3 and BaB_3C_3 stems from the couplings between C-2p orbitals and the boron E_g phonon modes.

Through MLWFs-based interpolation, we can obtain the accurate isotropic Eliashberg spectral function $\alpha^2F(\omega)$ for SrB_3C_3, as shown in Fig. 4(a). There are three peaks for $\alpha^2F(\omega)$. According to the peak position, $\alpha^2F(\omega)$ can be divided into three regions, i.e., [25 meV, 50 meV], [50 meV, 80 meV], and [80 meV, 105 meV]. The highest peak locates around 70 meV, resulted from the strongly coupled E_g modes. The tiny proportion of $\alpha^2F(\omega)$ below 25 meV

indicates that Sr-associated phonons have weak couplings with electrons, self-consistently with Fig. 3(a), in which the strongly coupled phonons mainly locate above the frequency gap. By integrating $\alpha^2F(\omega)$, we find that the EPC constant λ and logarithmic average frequency $\omega_{\log}$ are equal to 0.92 and 46.87 meV, respectively. Utilizing the so-called McMillian-Allen-Dynes formula [31] and setting the screened Coulomb potential μ^* to 0.1, the T_c of SrB_3C_3 is computed to be 32.9 K. As shown in Figs. 2(c)–2(e), the anisotropic of $\lambda_{\mathbf{k}n}$ cannot be neglected. It is more reasonable to determine the T_c by solving the anisotropic Eliashberg equations. The normalized density of superconducting gap $\Delta_{\mathbf{k}n}$, i.e., $\rho(\Delta_{\mathbf{k}n})$, at each temperature is given in Fig. 4(b). At 5 K, the average $\Delta_{\mathbf{k}n}$ is 6.31 meV. From our calculation, the anisotropy ratio of superconducting gap, Δ^{aniso}, defined by $(\Delta^{\max}\text{-}\Delta^{\min})/\Delta^{\text{ave}} = (7.29\text{-}5.22)/6.31 = 32.8\%$. The highest temperature with nonvanished $\Delta_{\mathbf{k}n}$ corresponds to the superconducting transition temperature, which is determined to be 40 K for SrB_3C_3, slightly higher than in MgB_2. The distribution of $\Delta_{\mathbf{k}n}$ on Fermi surfaces [Figs. 4(e)–4(g)] exhibits similar characteristics of $\lambda_{\mathbf{k}n}$ [Figs. 2(c)–2(e)]. Hence, SrB_3C_3 is a phonon-mediated high-T_c anisotropic s-wave superconductor. It is obvious that the McMillian-Allen-Dynes formula underestimates T_c by 18.0%. It is noticed that the McMillian-Allen-Dynes T_c was overestimated to 42 K at ambient pressure [24]. To identify the role of Sr phonons in EPC, the remanent λ equals 0.79 if we neglect the Sr phonons. The T_c determined by solving the anisotropic Eliashberg equations is slightly reduced to 38 K.

Since phonon softening is propitious to conventional superconductivity, the replacement of Sr with Ba can weaken the interatomic force constants. As a consequence, both the phonon DOS and $\alpha^2F(\omega)$ are redshifted, especially the main peak of $\alpha^2F(\omega)$ [Fig. 4(c)]. Interestingly, the triple-peak behavior for $\alpha^2F(\omega)$ of SrB_3C_3 disappears in BaB_3C_3, giving rise to a single broadening peak. The EPC constant λ, $\omega_{\log}$, and McMillian-Allen-Dynes T_c are found to be 0.96, 48.53 meV, and 36.6 K, respectively. Generally, phonon softening will lead to enhanced λ and reduced $\omega_{\log}$ [32]. As we see, the peak in interval [25 meV, 50 meV] exhibits significant blueshift, which can account for the abnormal aggrandizement of $\omega_{\log}$. As expected, BaB_3C_3 has an improved T_c of 43 K [Fig. 4(d)]. Similarly, the Δ^{aniso}=(8.27–5.81)/7.09=34.7%, slightly enlarged with respect to SrB_3C_3. By neglecting the Ba phonons, we find that λ and T_c are equal to 0.86 and 42 K for BaB_3C_3, respectively. These observations mean that Sr and Ba have little impact on the EPC and superconductivity.

There are two possible reasons for the enhancement of λ in BaB_3C_3, i.e., softened phonons and enlarged $N(0)$. To clarify which factor plays a dominant role, we further calculated the Fermi surface nesting function $\xi(\mathbf{q})$, EPC matrix element weighted nesting function $\gamma(\mathbf{q})$, and $\mathbf{q}$-resolved EPC constant $\lambda(\mathbf{q})$. $\xi(\mathbf{q})$ and $\gamma(\mathbf{q})$ are computed through

$$\xi(\mathbf{q}) = \frac{1}{N(0)N_{\mathbf{k}}}\sum_{nm\mathbf{k}}\delta\left(\epsilon^n_{\mathbf{k}}\right)\delta\left(\epsilon^m_{\mathbf{k}+\mathbf{q}}\right), \tag{1}$$

and

$$\gamma(\mathbf{q}) = \frac{1}{N(0)N_{\mathbf{k}}}\sum_{nm\mathbf{k}\nu}\left|g^{nm}_{\mathbf{k},\mathbf{q}\nu}\right|^2\delta\left(\epsilon^n_{\mathbf{k}}\right)\delta\left(\epsilon^m_{\mathbf{k}+\mathbf{q}}\right), \tag{2}$$

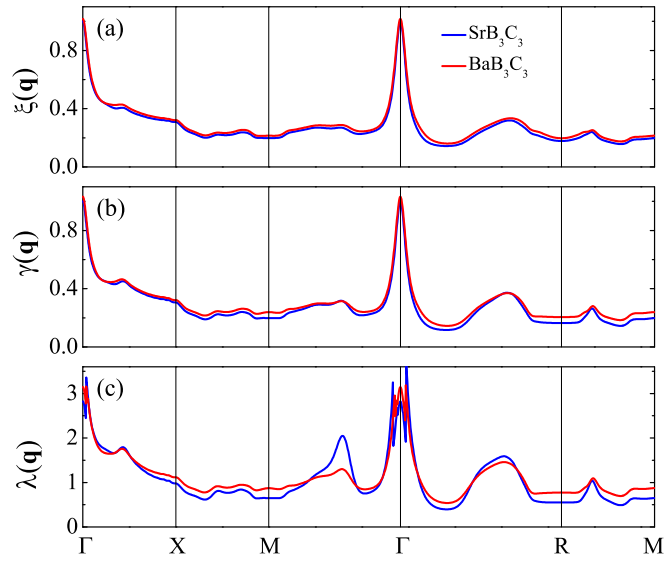

FIG. 5. Comparisons of nesting function $\xi(\mathbf{q})$, EPC matrix element weighted nesting function $\gamma(\mathbf{q})$, and $\mathbf{q}$-resolved EPC constant $\lambda(\mathbf{q})$ for SrB_3C_3 and BaB_3C_3. In these two compounds, $\xi(\mathbf{q})$ and $\gamma(\mathbf{q})$ are respectively normalized by $\xi(\Gamma)$ and $\gamma(\Gamma)$ of SrB_3C_3.

respectively. Here $\omega_{\mathbf{q}\nu}$ corresponds the phonon frequency and $g^{nm}_{\mathbf{k},\mathbf{q}\nu}$ represents the EPC matrix element. (n, m) and ν denote the indices of energy bands and phonon mode, respectively. $\epsilon^n_{\mathbf{k}}$ and $\epsilon^m_{\mathbf{k}+\mathbf{q}}$ are the eigenvalues of the electronic states with respect to the Fermi energy. $N_{\mathbf{k}}$ is the total number of $\mathbf{k}$ points in the fine mesh. $\lambda(\mathbf{q}) = \sum_\nu \lambda_{\mathbf{q}\nu}$, in which $\lambda_{\mathbf{q}\nu}$ reads

$$\lambda_{\mathbf{q}\nu} = \frac{2}{\hbar N(0)N_{\mathbf{k}}}\sum_{nm\mathbf{k}}\frac{1}{\omega_{\mathbf{q}\nu}}\left|g^{nm}_{\mathbf{k},\mathbf{q}\nu}\right|^2\delta\left(\epsilon^n_{\mathbf{k}}\right)\delta\left(\epsilon^m_{\mathbf{k}+\mathbf{q}}\right). \tag{3}$$

Although $N(0)$ of BaB_3C_3 is slightly larger than that of SrB_3C_3, the nesting functions in these two compounds are almost indistinguishable [Fig. 5(a)]. This clearly suggests that the variations of $N(0)$ and Fermi surfaces are not the major factors that affect λ. Compared with $\xi(\mathbf{q})$, the discrepancy in $\gamma(\mathbf{q})$ is visible between these two compounds [Fig. 5(b)]. The gap in $\lambda(\mathbf{q})$ is further amplified with respect to $\gamma(\mathbf{q})$, especially along the X-M and the R-M lines [Fig. 5(c)]. As a result, $\lambda(\mathbf{q})$ of BaB_3C_3 overwhelms that of SrB_3C_3. The only difference between $\gamma(\mathbf{q})$ and $\lambda(\mathbf{q})$ comes from the denominator $\omega_{\mathbf{q}\nu}$, according to Eq. (2) and Eq. (3). If the strongly coupled phonon mode has a relatively lower frequency, the aggrandizement of $\lambda(\mathbf{q})$ will be obtained. Thus, the behaviors of $\gamma(\mathbf{q})$ and $\lambda(\mathbf{q})$ strongly suggest that the softened phonons can account for the increase of λ in BaB_3C_3. As we see, there is a peak in $\lambda(\mathbf{q})$ near the middle region between M and Γ points for SrB_3C_3. This is closed related to the strongly coupled acoustic phonons, which are absent in BaB_3C_3 [Figs. 3(a) and 3(b)].

III. CONCLUSION

In summary, we have presented the first-principles calculations of electronic structure, lattice dynamics, and EPC for recently synthesized carbon-boron clathrate SrB_3C_3. The EPC strength λ is accurately determined as strong as 0.92,

based on state-of-the-art Wannier interpolation technique. We find that the strong coupling between C-2p orbitals and boron E_g phonon modes can pair electrons into a high-T_c state. By taking the anisotropy of Fermi surface into consideration, the superconducting transition temperature is calculated to be 40 K after solving the anisotropic Eliashberg equations. Furthermore, the T_c can be further boosted to 43 K by substituting Ba for Sr, resulted from softened phonons. At 5 K, the anisotropic ratios of superconducting gap on the Fermi surface are 32.8% and 34.7% for SrB_3C_3 and BaB_3C_3, respectively. Thus, these two compounds are phonon-mediated high-T_c anisotropic s-wave superconductors.

ACKNOWLEDGMENTS

This work was supported by the National Natural Science Foundation of China (Grants No. 11974194 and No. 11974207). M.G. was also sponsored by K. C. Wong Magna Fund in Ningbo University.

APPENDIX A: COMPUTATIONAL METHODS

In our calculations, the first-principles package, QUANTUM-ESPRESSO, was adopted [33]. We calculated the electronic states and phonon perturbation potentials [34] using the generalized gradient approximation (GGA) of Perdew-Burke-Ernzerhof formula [35] and the optimized norm-conserving Vanderbilt pseudopotentials [36]. After the convergence test, the kinetic energy cutoff and the charge density cutoff were chosen to be 80 Ry and 320 Ry, respectively. The charge densities were calculated on an unshifted **k** mesh of 16×16×16 points in combination with a Methfessel-Paxton smearing [37] of 0.02 Ry. The dynamical matrices and the perturbation potentials were computed on a Γ-centered 4×4×4 mesh, within the framework of density-functional perturbation theory [38].

For SrB_3C_3, we chose 24 sp^3-hybridized states localized in the middle of boron-carbon bonds as the initial guess to construct the maximally localized Wannier functions (MLWFs) [39]. In addition to these sp^3-hybridized states, the 5p orbitals of Ba were also included during the generation of MLWFs for BaB_3C_3. After optimization, these MLWFs exhibit excellent localization in space. For example, the average spatial spread of MLWFs for SrB_3C_3 and BaB_3C_3 are 1.50 Å^2 and 1.21 Å^2, respectively. The convergence test for EPC constant λ was carried out through fine electron (60×60×60) and phonon (20×20×20) grids with EPW codes [40]. The Dirac δ functions for electrons and phonons were smeared out by a Gaussian function with the widths of 100 meV and 0.5 meV, respectively. A fine electron grid of 40×40×40 points was employed in solving the anisotropic Eliashberg equations. The sum over Matsubara frequencies was truncated with $\omega_c = 1.0$ eV, about ten times that of the highest phonon frequency. For the methodology of solving anisotropic Eliashberg equations, please see Refs. [22,23,40].

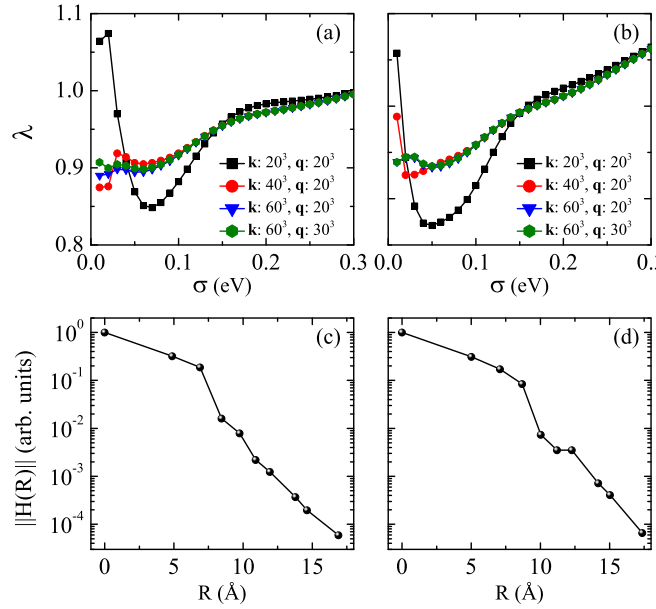

FIG. 6. Convergence test of EPC constant λ for SrB_3C_3 (a) and BaB_3C_3 (b). Spatial decay of electronic Hamiltonian in the Wannier representation for SrB_3C_3 (c) and BaB_3C_3 (d). Here, the absolute value of hopping integral of the Hamiltonian is normalized by the maximal one.

APPENDIX B: CONVERGENCE TEST OF EPC CONSTANT λ AND LOCALIZATION OF CONSTRUCTED HAMILTONIAN IN WANNIER REPRESENTATION

For SrB_3C_3 and BaB_3C_3, the convergence tests for EPC constant λ versus the density of **k** mesh are shown in Figs. 6(a) and 6(b). Here, we chose three different **k** meshes for the Brillouin zone sampling, i.e., 20×20×20, 40×40×40, and 60×60×60. We also extended the **q** mesh from 20×20×20 points to 30×30×30 points to test the convergence. For large smearing width σ, the curves given by these three **k** meshes coincide. When approaching the limit of $\sigma \to 0$, the separation for λ determined by **k** meshes of 40×40×40 and 60×60×60 occurs at $\sigma = 0.1$ eV. This indicates that **k** mesh of 60×60×60 points can give rise to a convergent EPC constant λ for σ being 0.1 eV. Since the accuracy of Wannier interpolation strongly relies on the localization of constructed Hamiltonian in the Wannier representation, we also carefully checked the spatial decay of hopping integrals for real-space Hamiltonian [Figs. 6(c) and 6(d)]. The absolute value of the hopping integral exhibits exponential decay. As mentioned in the methods section, a **k** mesh of 4×4×4 points was adopted during the construction of MLWFs. This means that the length of cubic crystal that we calculated is about 19.5 Å with periodic boundary condition. According to Fig. 6(c), the hopping integral already decreases to 5.9×10^{-5} for $R = 16.9$ Å. This guarantees the accuracy of Wannier-based interpolation.

[1] N. W. Ashcroft and N. D. Mermin, *Solid State Physics* (Holt, Rinehart, and Winston, New York, 1976).

[2] E. A. Ekimov, V. A. Sidorov, E. D. Bauer, N. N. Mel'nik, N. J. Curro, J. D. Thompson, and S. M. Stishov, Nature (London) **428**, 542 (2004).

[3] T. Yokoya, T. Nakamura, T. Matsushita, T. Muro, Y. Takano, M. Nagao, T. Takenouchi, H. Kawarada, and T. Oguchi, Nature (London) **438**, 647 (2005).

[4] L. Boeri, J. Kortus, and O. K. Andersen, Phys. Rev. Lett. **93**, 237002 (2004).

[5] K.-W. Lee and W. E. Pickett, Phys. Rev. Lett. **93**, 237003 (2004).

[6] X. Blase, Ch. Adessi, and D. Connétable, Phys. Rev. Lett. **93**, 237004 (2004).

[7] H. J. Xiang, Z. Li, J. Yang, J. G. Hou, and Q. Zhu, Phys. Rev. B **70**, 212504 (2004).

[8] J. E. Moussa and M. L. Cohen, Phys. Rev. B **77**, 064518 (2008).

[9] Y. Takano, T. Takenouchi, S. Ishii, S. Ueda, T. Okutsu, I. Sakaguchi, H. Umezawa, H. Kawarada, and M. Tachiki, Diamond Relat. Mater. **16**, 911 (2007).

[10] Z.-F. Ouyang, X.-W. Yan, and M. Gao, Appl. Phys. Express **13**, 083003 (2020).

[11] V. L. Solozhenko, O. O. Kurakevych, D. Andrault, Y. Le Godec, and M. Mezouar, Phys. Rev. Lett. **102**, 015506 (2009).

[12] P. V. Zinin, L. C. Ming, H. A. Ishii, R. Jia, T. Acosta, and E. Hellebrand, J. Appl. Phys. **111**, 114905 (2015).

[13] J. S. Kasper, P. Hagenmuller, M. Pouchard, and C. Cros, Science **150**, 1713 (1965).

[14] H. Kawaji, H.-o. Horie, S. Yamanaka, and M. Ishikawa, Phys. Rev. Lett. **74**, 1427 (1995).

[15] D. Connétable, V. Timoshevskii, B. Masenelli, J. Beille, J. Marcus, B. Barbara, A. M. Saitta, G.-M. Rignanese, P. Mélinon, S. Yamanaka, and X. Blase, Phys. Rev. Lett. **91**, 247001 (2003).

[16] K. Tanigaki, T. Shimizu, K. M. Itoh, J. Teraoka, Y. Moritomo, and S. Yamanaka, Nat. Mater. **2**, 653 (2003).

[17] I. Spagnolatti, M. Bernasconi, and G. Benedek, Eur. Phys. J. B **34**, 63 (2003).

[18] F. Zipoli, M. Bernasconi, and G. Benedek, Phys. Rev. B **74**, 205408 (2006).

[19] Y. Wang, J. Lv, L. Zhu, and Y. Ma, Phys. Rev. B **82**, 094116 (2010).

[20] L. Zhu, G. M. Borstad, H. Liu, P. A. Guńka, M. Guerette, J.-A. Dolyniuk, Y. Meng, E. Greenberg, V. B. Prakapenka, B. L. Chaloux, A. Epshteyn, R. E. Cohen, and T. A. Strobel, Sci. Adv. **6**, eaay8361 (2020).

[21] H. J. Choi, D. Roundy, H. Sun, M. L. Cohen, and S. G. Louie, Nature (London) **418**, 758 (2002).

[22] H. J. Choi, M. L. Cohen, and S. G. Louie, Physica C **385**, 66 (2003).

[23] E. R. Margine and F. Giustino, Phys. Rev. B **87**, 024505 (2013).

[24] L. Zhu, H. Liu, R. E. Cohen, R. Hoffmann, and T. A. Strobel, arXiv:1708.03483.

[25] J. Kortus, I. I. Mazin, K. D. Belashchenko, V. P. Antropov, and L. L. Boyer, Phys. Rev. Lett. **86**, 4656 (2001).

[26] Y. Kong, O. V. Dolgov, O. Jepsen, and O. K. Andersen, Phys. Rev. B **64**, 020501(R) (2001).

[27] D. W. Boukhvalov, M. I. Katsnelson, and A. I. Lichtenstein, Phys. Rev. B **77**, 035427 (2008).

[28] H. Tang and S. Ismail-Beigi, Phys. Rev. Lett. **99**, 115501 (2007).

[29] W. Li, L. Kong, C. Chen, J. Gou, S. Sheng, W. Zhang, H. Li, L. Chen, P. Cheng, and K. Wu, Sci. Bull. **63**, 282 (2018).

[30] M. Gao, X.-W. Yan, J. Wang, Z.-Y. Lu, and T. Xiang, Phys. Rev. B **100**, 024503 (2019).

[31] P. B. Allen and R. C. Dynes, Phys. Rev. B **12**, 905 (1975).

[32] X.-T. Jin, X.-W. Yan, and M. Gao, Phys. Rev. B **101**, 134518 (2020).

[33] P. Giannozzi, S. Baroni, N. Bonini, M. Calandra, R. Car, C. Cavazzoni, D. Ceresoli, G. L. Chiarotti, M. Cococcioni, I. Dabo, A. Dal Corsol, S. de Gironcoli, S. Fabris, G. Fratesi, R. Gebauer, U. Gerstmann, C. Gougoussis, A. Kokalj, M. Lazzeri, L. Martin-Samos, N. Marzari, F. Mauri, R. Mazzarello, S. Paolini, A. Pasquarello, L. Paulatto, C. Sbraccia, S. Scandolo, G. Sclauzero, A. P. Seitsonen, A. Smogunov, P. Umari, and R. M. Wentzcovitch, J. Phys.: Condens. Matter **21**, 395502 (2009).

[34] F. Giustino, M. L. Cohen, and S. G. Louie, Phys. Rev. B **76**, 165108 (2007).

[35] J. P. Perdew, K. Burke, and M. Ernzerhof, Phys. Rev. Lett. **77**, 3865 (1996).

[36] D. R. Hamann, Phys. Rev. B **88**, 085117 (2013).

[37] M. Methfessel and A. T. Paxton, Phys. Rev. B **40**, 3616 (1989).

[38] S. Baroni, S. de Gironcoli, A. Dal Corso, and P. Giannozzi, Rev. Mod. Phys. **73**, 515 (2001).

[39] G. Pizzi, V. Vitale, R. Arita, S. Blügel, F. Freimuth, G. Granton, M. Gibertini, D. Gresch, C. Johnson, T. Koretsune, J. Ibañez-Azpiroz, H. Lee, J.-M. Lihm, D. Marchand, A. Marrazzo, Y. Mokrousov, J. I. Mustafa, Y. Nohara, Y. Nomura, L. Paulatto, S. Poncé, T. Ponweiser, J. Qiao, F. Thöle, S. S. Tsirkin, M. Wierzbowska, N. Marzari, D. Vanderbilt, I. Souza, A. A. Mostofi, and J. R. Yates, J. Phys.: Condens. Matter **32**, 165902 (2020).

[40] S. Poncé, E. R. Margine, C. Verdi, and F. Giustino, Comp. Phys. Commun. **209**, 116 (2016).